

IDENTIFICATION, CONTROL AND HYSTERESIS COMPENSATION OF A 3 DOF METROLOGICAL AFM

Roel Merry, Mustafa Uyanik, René van de Molengraft, Richard Koops,
Marijn van Veghel, and Maarten Steinbuch

ABSTRACT

Atomic Force Microscopes (AFMs) are widely used for the investigation of samples at the nanometer scale. The metrological AFM used in this work uses a 3 degrees-of-freedom (DOFs) stage, driven by piezo-stack actuators, for sample manipulation in combination with a fixed cantilever. The piezo-stack actuators suffer from hysteresis, which acts as a nonlinear disturbance on the system and/or can change the system dynamics. The contributions of this paper are the application of feedback control to all 3 DOFs of the metrological AFM and the design and application of a hysteresis feedforward for the asymmetric hysteresis present in the system. The amount of coupling between the DOFs is assessed by a non-parametric multiple-input-multiple-output (MIMO) identification. Since the dynamics appear to be decoupled in the frequency range of interest, feedback controllers are designed for each DOF separately. For the modeling of the asymmetric hysteresis an extended Coleman-Hodgdon model is proposed. This model is used for feedforward compensation of the hysteresis. The combination of feedback control for all DOFs and the asymmetric hysteresis feedforward enables the AFM to track scanning profiles within the sensor bound of 5 nm. Real-time imaging of the sample is possible with an accuracy of 2 nm.

Key Words: Scanning microscopes, motion control, asymmetric hysteresis, piezo actuators, MIMO identification.

I. INTRODUCTION

Atomic force microscopes (AFMs) are a specific type of scanning probe microscopes (SPMs) in which the surface of a sample is scanned by a very sharp probe.

Manuscript received February 7, 2008; accepted August 8, 2008.

R.J.E. Merry, M. Uyanik, M.J.G. van de Molengraft and M. Steinbuch are with the Eindhoven University of Technology, Department of Mechanical Engineering, Control Systems Technology Group, P.O. Box 513, 5600 MB Eindhoven, The Netherlands (e-mail: r.j.e.merry@tue.nl).

K.R. Koops and M.G.A. van Veghel are with NMI Van Swinderen Laboratorium, Thijssseweg 11, 2629 JA Delft, The Netherlands.

The sample to be investigated can either be moved under the probe (scanning sample mode) or the probe can be moved over the sample (scanning tip mode). The sample causes the cantilever, to which the tip is attached, to deflect. The deflection can be used to obtain the height information of the sample. The atomic force microscope was invented in 1986 by Binnig, Quate and Gerber [1] and is widely used for sample imaging, the characterization of materials and the manipulation of particles at nanometer scale [2].

In this paper, a metrological AFM is considered. The metrological AFM is used to calibrate transfer standards for commercial AFMs. In contrast to commercial AFMs, the accuracy of the measurements is much more important than the scanning speed. Furthermore, the measurements have to be traceable to the standard

of length. This imposes different constraints on both the mechanical and control design of the AFM.

In current AFMs, the positioning of the sample under the probe, *i.e.* the scanning motion in x and y direction, is often done using piezoelectric actuators in an open-loop manner [3, 4]. Examples of these techniques are H_∞ based [4–6] and model inverse based [7] feed-forward control. However, due to the presence of disturbances in AFMs the performance can benefit from applying feedback control in the scanning directions [2]. Another issue is that the piezoelectric actuators exhibit nonlinear behavior such as hysteresis and creep, which limit the positioning accuracy of the sample. Furthermore, the manipulation of samples in multiple degrees-of-freedom (DOFs) inherently makes the AFM a multiple-input-multiple-output (MIMO) control system. The increasing interest in AFMs for nano-applications requires a higher precision and therefore an increasing closed-loop bandwidth for disturbance attenuation.

During the last decades a lot of research on the design, operating mode and control of AFMs has been done. The sample manipulation is often performed using tube piezo actuators [8], which can move the sample in three directions using one actuator. The lateral bending of the piezo-tubes results in a large cross coupling to the vertical direction, which distorts the image of the AFM. Tripod scanners employ three piezoelectric stack actuators, one for each translational axis [1]. The path lengths are determined by the length of the stack piezos, resulting in either a small range or in low-frequency mechanical resonances and thus low speeds [2]. Resonant scanners use an oscillating tuning fork as actuator to obtain fast scanning [9]. However, the scan rate is dependent on the resonance frequency of the tuning fork and cannot be chosen independently. Stages where the piezo-actuators for the various degrees-of-freedom (DOFs) are stacked on top of each other typically have a large moving mass, which results in a low-frequency first resonance and low scanning speed [10]. Rigid scanners combine piezoelectric stack actuators with a flexure mechanism [11, 12], which decouples the different axes of motion to a large extent in combination with a high performance. In this paper, a 3 DOF rigid scanner driven by three piezoelectric stack actuators is used [13].

Probing of the sample surface can be performed in contact or tapping mode. In this paper we will only consider contact scanning, in which the tip and sample are in contact at all times. The image of the sample is commonly retrieved based on the control effort of the actuator in the imaging z direction. The deflection of the tip can be controlled either in constant force

mode, where the force between the sample and the tip is held constant, or in constant height mode, where the feedback is disabled completely [14]. The constant height mode allows for faster imaging, but the varying force can damage the sample and/or tip. The constant force mode gives a high resolution, but only at low speed. In this paper, we use constant force scanning in combination with a scanning sample mode to obtain a fully traceable image of the sample.

SPM stages are mostly designed to minimize coupling between the different DOFs, especially with respect to the imaging z axis. However, practically always an amount of coupling is present, *e.g.* due to alignment errors or manufacturing tolerances. In the literature, the AFMs are mainly identified and modeled as three separate single-input-single-output (SISO) systems in x , y (scanning motion) and z (imaging) directions. For control design purposes the MIMO aspects are commonly disregarded without justification [3]. MIMO identification of the scanning motion only is performed for a tube piezoelectric actuator in [8] and for a 2 DOF nanopositioner driven by piezo-stack actuators in [4]. The coupling to the imaging z axis is not taken into account. In this paper, a full MIMO identification in all three directions is performed and the coupling effects between the various axes are assessed.

The asymmetry in the used 3 DOF rigid scanner results in an asymmetric hysteresis in the system [15]. The hysteresis in the metrological AFM shows an asymmetry between increasing and decreasing voltage paths and different offsets for various voltage ranges. In the literature, several models and methods are proposed for asymmetric hysteresis. An extended Preisach model for asymmetric hysteresis requires 80 parameters to be identified [16], which makes it difficult and time consuming to find a general model for the complete operating range. Separate Preisach models for each voltage range are identified in [17]. For the compensation, switches between a large number of models have to be made based on the different parts in the reference trajectory. A Bouc-Wen model, using only 9 parameters, is identified in [18] using genetic algorithms. However, the model only incorporates asymmetry near zero velocity of the stage. A Bouc-Wen model for symmetric hysteresis is combined to a PI feedback compensation for the asymmetric part in [19], which does not utilize the a-priori knowledge about the asymmetry. A generalized Bouc-Wen model which splits the hysteresis in 6 different parts requires a lot of parameters for the identification and a lot of switches between different models during the compensation [15]. In [20], a Coleman-Hodgdon model is proposed for the modeling and compensation of symmetric hysteresis in a scanning

microscope. The model only requires 5 parameters to be identified. The variations in the offset for various voltage ranges are included in an enhanced Coleman-Hodgdon model in [21]. However, for each voltage range a new model has to be identified. In this paper, an extended Coleman-Hodgdon model is proposed to incorporate the variations in the offset. Furthermore, different models are identified for increasing and decreasing voltages. For the feedforward compensation, this requires only a switch between two models at standstill of the stage.

The contributions of this paper are threefold. Firstly, we justify SISO-based controller design by assessing the amount of coupling between the three axes. Secondly, feedback control is applied to all 3 DOFs, so also to the scanning motion. Loopshaping techniques have been employed to tune three feedback controllers at bandwidths below which the coupling effects can be neglected. Finally, an extended Coleman-Hodgdon model is proposed to model the asymmetric hysteresis in the system. With the proposed model, a hysteresis feedforward is added, which efficiently compensates hysteretic disturbances in the system. The combination of feedback control and hysteresis feedforward control allows the sample to be positioned with a tracking error within the sensor bound of 5 nm.

This paper is organized as follows. In Section II, the metrological AFM is discussed in more detail. In Section III, MIMO identification is used to assess the amount of coupling between the various axes of the AFM. The extended Coleman-Hodgdon model to describe the asymmetric hysteresis is also discussed in Section III. The design of the feedback and hysteresis feedforward controllers is presented in Section IV. The results of the experiments with the metrological AFM are shown in Section V. Finally, conclusions are drawn in Section VI.

II. METROLOGICAL AFM

The metrological AFM, shown in Fig. 1, consists of an Topometrix AFM head, a piezo-stack driven 3 DOF stage and a ZYGO interferometer to measure the stage position in all DOFs. The PI P517.3CL 3 DOF stage [13] is a rigid stage containing three piezo-stack actuators, which can move the stage through a flexure mechanism in a range of 100 μm in x and y directions and in a range of 20 μm in z direction. The PI 3 DOF stage is designed to minimize the amount of coupling between the different DOFs, especially to the imaging z axis. Furthermore, in each direction it has an angular deviation of maximum 2 arcsec over the entire range. A

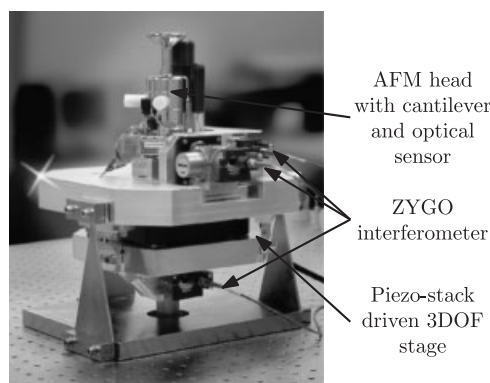


Fig. 1. Picture of the metrological AFM containing a Topometrix AFM head, a piezo-stack driven 3 DOF PI P517.3CL stage and a ZYGO interferometer.

Table I. Resolution and noise bound of the different sensors.

Sensor	Resolution	Noise bound
ZYGO x	0.15 nm	± 5 nm
ZYGO y	0.15 nm	± 4 nm
ZYGO z	0.15 nm	± 2 nm
Head z	0.05 nm	± 0.15 nm

mapping as function of the position can be made to correct for this small deviation, thus eliminating the need for a full 6 DOF stage. The mirrors and lasers of the interferometer are aligned such that the laser spots in all DOFs are exactly aligned with the tip of the cantilever. This eliminates Abbe errors, *i.e.* a change in orientation between the sample and tip of the cantilever does not affect the measurements of the ZYGO interferometers. The deflection of the cantilever in the AFM head is measured by an optical sensor consisting of a laser and a photodiode. The measurement resolution of the ZYGO interferometer equals 0.15 nm in all directions. The cantilever deflection can be measured with a resolution of 0.05 nm. The resolution and noise bounds of the different sensors are given in Table I. The noise bound is defined as the measured output range of the sensors when the stage is at standstill and the input to the piezo actuators is decoupled.

A schematic representation of the AFM and the feedback control loop is shown in Fig. 2. For clarity the flexure mechanisms between the piezo-stack actuators and the stage are not shown. Feedback control is applied in x and y directions by steering the piezo-stack actuators using the ZYGO position measurements. In z direction, the tip is controlled in constant force mode while the stage with the sample is moved in 3 DOFs under the cantilever. The setpoint to the cantilever is a constant deflection, which is realized by moving the

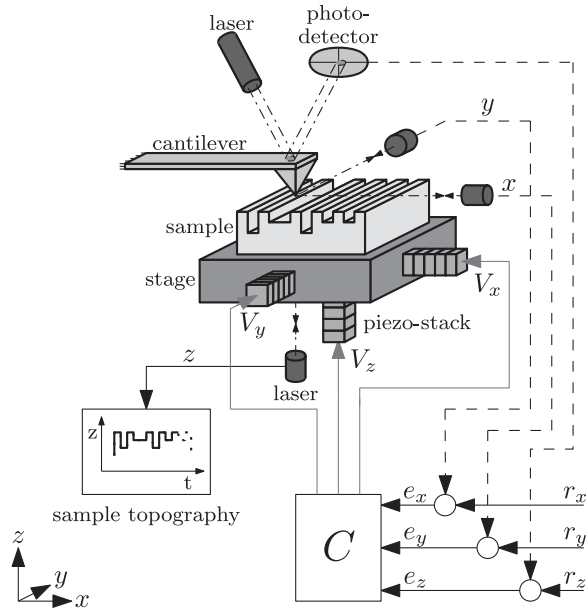


Fig. 2. Schematic representation of the AFM and the feedback control. Each DOF is driven by a piezo-stack actuator, thus minimizing the amount of coupling. The ZYGO laser interferometers are aligned on the cantilever tip to eliminate Abbe errors. The sample topography is measured directly by the interferometer in z direction.

stage in z direction. Keeping the deflection of the cantilever constant has the advantage that the orientation of the tip compared to the sample topography remains constant. Also Abbe errors and errors due to the uncertainty in the sensitivity of the cantilever are eliminated in this way. Since the tip is controlled to a constant deflection, the laser of the head cannot be used to obtain the sample topography. Instead of using the control effort in z direction, the height of the sample is measured directly using the ZYGO interferometer in z direction. Since the stage position in x and y directions is directly traceable to the standard of length, the image of the sample topography can be constructed using all three ZYGO interferometer measurements.

The piezoelectric actuators in the 3 DOF stage suffer from hysteresis, which act as nonlinear disturbances on the system and/or change the system dynamics. Hysteresis can contribute to loss of robustness, performance degradation or instabilities in feedback controlled piezoelectric devices [22]. The measured hysteresis in the system is shown in Fig. 3 for separate symmetric scans in x direction and voltage ranges $\bar{V}_R \in \{2, 10, 20, 40, 60, 80, 100\}$ V while controlling the stage in y and z direction to a constant value.

In Fig. 3 can be seen that the level of hysteretic distortion varies depending on the maximum value of the input voltage. Let for each voltage range V_R the

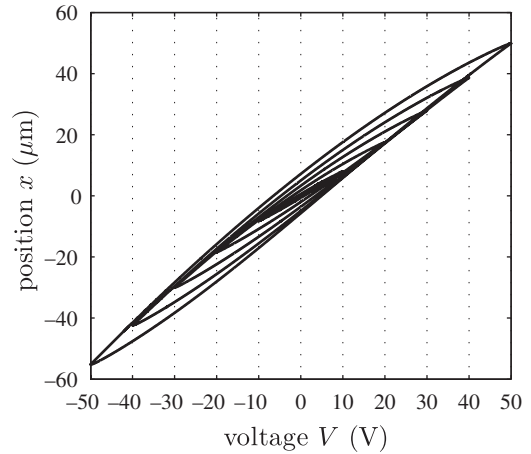


Fig. 3. Measured hysteresis for various voltage ranges. The hysteresis curves are asymmetric with respect to the trace and retrace direction. The offset of the hysteresis curves is dependent on the voltage range.

offset ε be defined as

$$\varepsilon(V_R) = \frac{1}{2}(V_M(V_R) - V_m(V_R)),$$

where V_M is the maximum voltage and V_m is the minimum voltage, *e.g.* for the voltage range $V_R = 80$ V we have $V_m = -40$ V and $V_M = 40$ V. For the hysteresis curves of various voltage ranges V_R (Fig. 3), the offsets $\varepsilon(V_R)$ are not equal. Furthermore, the trace (increasing voltage) and retrace (decreasing voltage) directions of each hysteresis curve are different in shape. In order to compensate the hysteresis by means of feedforward control, a model that incorporates the voltage range dependent offset $\varepsilon(V_R)$ and the non-symmetry between the trace and retrace directions is derived in Section 3.2.

III. IDENTIFICATION

Although ideally the different axes of the 3 DOF stage are decoupled, practically a certain amount of cross coupling will still be present due to alignment errors or parasitic dynamics. In this section, non-parametric MIMO identification of the metrological AFM is performed to assess the amount of coupling between the various DOFs. Furthermore, an extended Coleman-Hodgdon model is proposed to model the asymmetric hysteresis.

3.1 MIMO identification

In order to investigate the amount of coupling between the different axes, full non-parametric MIMO identification of the system is performed. The system inputs are the voltages $V_i, i \in \{x, y, z\}$ to the piezo-stack

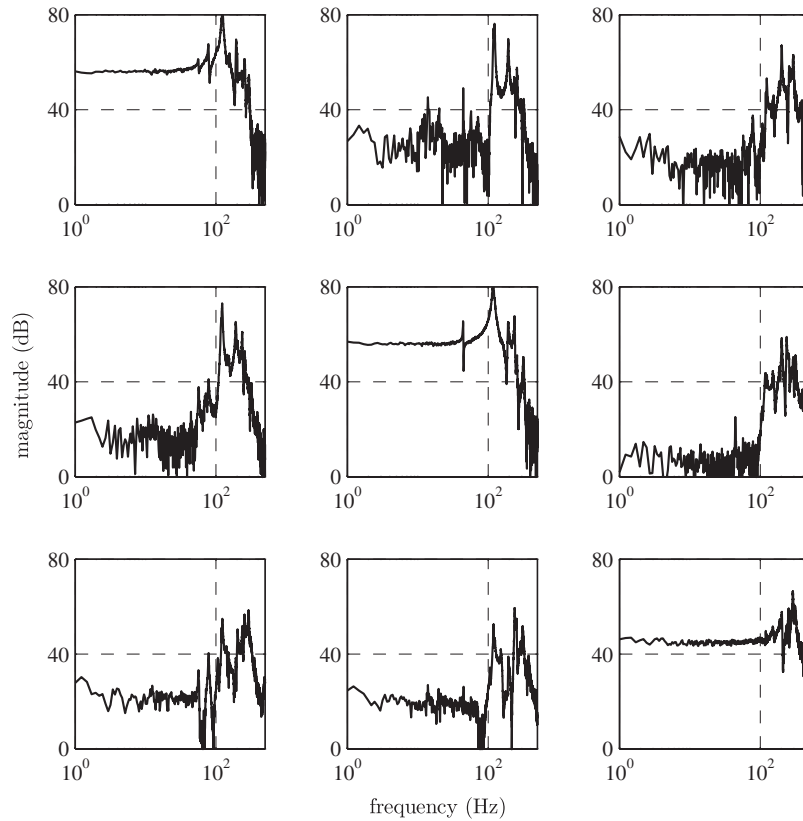


Fig. 4. Bode magnitude plots of the full MIMO system (1). Up to the first resonance at ± 40 Hz, the FRFs show a zero slope. For frequencies $f < 100$ Hz the magnitude of the off-diagonal terms is ± 40 dB lower than the magnitude of the diagonal terms.

actuators and the outputs are the position measurements of the ZYGO interferometer in x and y directions and of the optical sensor in the AFM head in z direction. The system can be written as

$$P(f) = \begin{bmatrix} P_{xx}(f) & P_{xy}(f) & P_{xz}(f) \\ P_{yx}(f) & P_{yy}(f) & P_{yz}(f) \\ P_{zx}(f) & P_{zy}(f) & P_{zz}(f) \end{bmatrix}, \quad (1)$$

where $P_{ji}(f)$ denotes the frequency response function (FRF) from the input V_i in direction i to the output in direction j as a function of the frequency f (Hz) and $i, j \in \{x, y, z\}$.

The different FRFs $P_{ji}(f)$ of (1) are determined using the non-parametric open-loop identification method and Welch's averaged periodogram method [23]. On each input independently a zero mean white noise signal with a variance of $\sigma^2 = 0.05 \text{ V}^2$ is applied while all outputs are measured. The Bode magnitude plots of the different FRFs are shown in Fig. 4. The FRFs show a zero slope at low frequencies. At frequencies $f \geq 40$ Hz several resonances can be seen. It can be seen that for frequencies $f < 100$ Hz the magnitude

of the off-diagonal FRFs is approximately 40 dB lower than the diagonal FRFs. For frequencies $f \geq 100$ Hz the amplitudes of all FRFs are in the same order of magnitude.

To investigate the amount of coupling between the different axes, the frequency-dependent relative gain array (RGA) [24, 25] of the non-singular square complex matrix $P(f)$ is calculated

$$\text{RGA}(P(f)) = P(f) \times (P(f)^{-1})^T, \quad (2)$$

where \times denotes element-wise multiplication. The rows and columns of the RGA sum to 1 for all frequencies f . The RGA provides a measure for the amount of interaction between the different axes. If the $\text{RGA}(f) = I$, $\forall f$, perfect decoupling is achieved. The RGA for the FRFs of Fig. 4 is shown in Fig. 5. It can be seen that for frequencies $f < 100$ Hz, the RGA is almost equal to the identity matrix. Therefore, for the purpose of feedback controller design the axes are assumed to be decoupled for frequencies up to 100 Hz. However, the small amount of coupling for $f < 100$ Hz will still affect the performance of the stage by approximately 1% (-40 dB) in an open loop manner. Possibly, this can

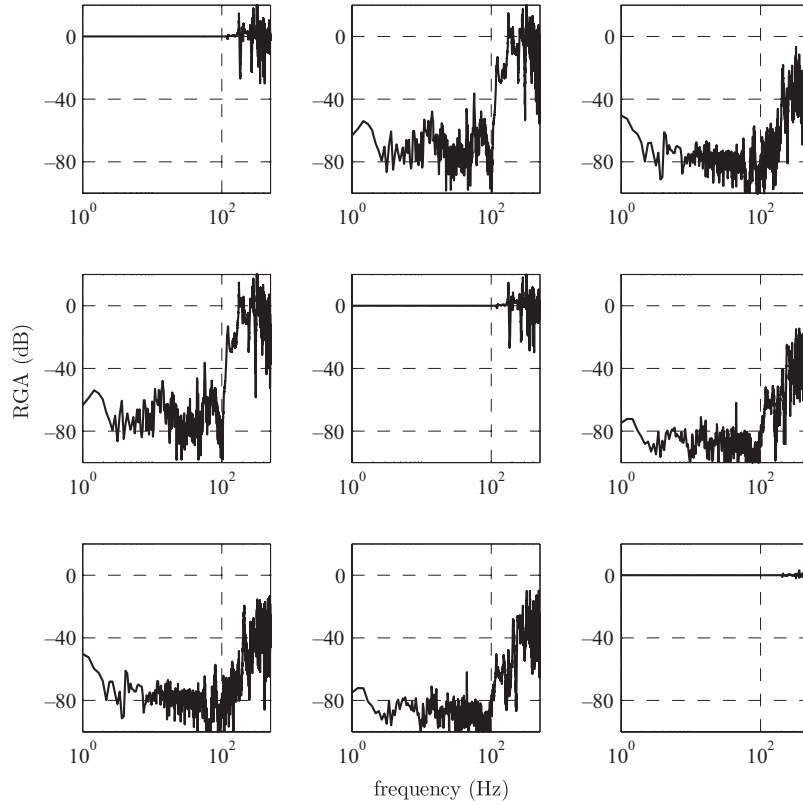


Fig. 5. RGA (2) of the full MIMO system (1). For frequencies $f < 100$ Hz, the RGA resembles an identity matrix and can be assumed decoupled. For frequencies $f \geq 100$ Hz the axes show a significant amount of coupling.

even be lower by the virtue of feedback. For frequencies $f \geq 100$ Hz, $RGA(f) \neq I$ as the axes are clearly coupled in this frequency range. Note that the coupling to the imaging z axis is still smaller than the coupling between the scanning x and y axes.

3.2 Hysteresis model

The Coleman-Hodgdon model was formulated in 1986 to describe rate-independent hysteresis in ferromagnetically soft materials [26]. In [20], the Coleman-Hodgdon model is applied successfully to describe the hysteresis in a scanning probe microscope driven by piezo actuators, *i.e.* the hysteresis between the applied voltage V and the resulting position x . For closed hysteresis loops, the position $x(V)$ can be described as

$$x(V) = \begin{cases} bV - \frac{b-u}{\alpha} \left(1 - \frac{2}{e^{-\alpha V_m} + e^{-\alpha V_M}} e^{-\alpha V} \right), & \text{if } \dot{V} \geq 0, \\ bV + \frac{b-u}{\alpha} \left(1 - \frac{2}{e^{\alpha V_m} + e^{\alpha V_M}} e^{\alpha V} \right), & \text{if } \dot{V} < 0, \end{cases} \quad (3)$$

where $\dot{V} = \frac{dV}{dt}$. The parameters b , $\alpha > 0$ and u are the constant parameters to be identified. The linear asymptote of the hysteresis curve has a slope determined by b and a position at 0 V of $\pm \frac{b-u}{\alpha}$ dependent on the scan direction.

The sensitivity of the hysteresis curve, bV in (3), is for the metrological AFM of Fig. 1 not linear as function of V_R [27]. Expansion of (3) with an exponential asymptotic sensitivity gives

$$x(V) = \begin{cases} (b - ae^{-cV_R})V - \frac{b-u}{\alpha} \\ \times \left(1 - \frac{2}{e^{-\alpha V_m} + e^{-\alpha V_M}} e^{-\alpha V} \right), & \text{if } \dot{V} \geq 0, \\ (b - ae^{-cV_R})V + \frac{b-u}{\alpha} \\ \times \left(1 - \frac{2}{e^{\alpha V_m} + e^{\alpha V_M}} e^{\alpha V} \right), & \text{if } \dot{V} < 0, \end{cases}$$

where the voltage range $V_R = V_M - V_m$. The above model does not incorporate any voltage range dependent offset $\varepsilon(V_R)$. Since the hysteresis in the metrological AFM shows an offset that is dependent on the voltage range V_R (see also Fig. 3) and because the trace and

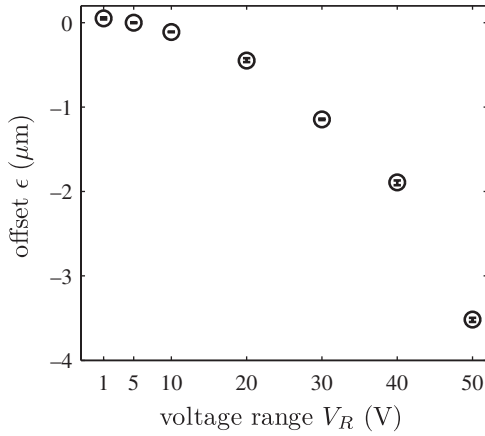


Fig. 6. Offset hysteresis curves versus voltage range. The offset changes quadratically with the voltage range.

retrace directions are not symmetrical, we propose an extended Coleman-Hodgdon model as

$$x(V) = \begin{cases} \varepsilon_t(V_R) + (b_t - a_t e^{-c_t V_R})V - \frac{b_t - u_t}{\alpha_t} \\ \quad \times \left(1 - \frac{2}{e^{-\alpha_t V_m} + e^{-\alpha_t V_M}} e^{-\alpha_t V} \right), & \text{if } \dot{V} \geq 0, \\ \varepsilon_r(V_R) + (b_r - a_r e^{-c_r V_R})V + \frac{b_r - u_r}{\alpha_r} \\ \quad \times \left(1 - \frac{2}{e^{\alpha_r V_m} + e^{\alpha_r V_M}} e^{\alpha_r V} \right), & \text{if } \dot{V} < 0, \end{cases} \quad (4)$$

where $\varepsilon_{t,r}(V_R)$ describes the voltage range dependent offset. The offset as a function of V_R is shown in Fig. 6. It can be seen that the offset changes quadratically with the voltage range. Therefore, the functions $\varepsilon_{t,r}(V_R)$ are chosen as

$$\varepsilon_t(V_R) = d_t V_R^2 + e_t V_R + f_t,$$

$$\varepsilon_r(V_R) = d_r V_R^2 + e_r V_R + f_r.$$

The identification of the model parameters $\{a, b, c, u, \alpha, d, e, f\}_{t,r}$ is done by means of an optimization over the measured first-order reversal hysteresis curves for various voltage ranges $V_R \in \{2, 10, 30, 40, 60, 80, 100\}$ V. The optimization is performed using a nonlinear least-squares data-fitting method because the model described by (4) is highly nonlinear. The initial parameters are chosen based on an explorative measurement in combination with the findings from [27]. For the trace x_t ($\dot{V} \geq 0$) and the

Table II. The identified parameters of the extended Coleman-Hodgdon model for both the trace and retrace directions.

Parameter	Value trace x_t	Value retrace x_r
a ($\mu\text{m}/\text{V}$)	2.6570×10^{-1}	3.0892×10^{-1}
c (V^{-1})	2.3318×10^{-2}	9.2649×10^{-2}
b ($\mu\text{m}/\text{V}$)	1.1530	1.3555
u ($\mu\text{m}/\text{V}$)	9.4970×10^{-1}	8.7338×10^{-1}
α (V^{-1})	5.5306×10^{-2}	2.5985×10^{-2}
d ($\mu\text{m}/\text{V}$)	-2.9444×10^{-4}	-3.0051×10^{-4}
e ($\mu\text{m}/\text{V}$)	-2.8998×10^{-3}	-1.4058×10^{-3}
f (μm)	6.2200×10^{-2}	8.4353×10^{-2}

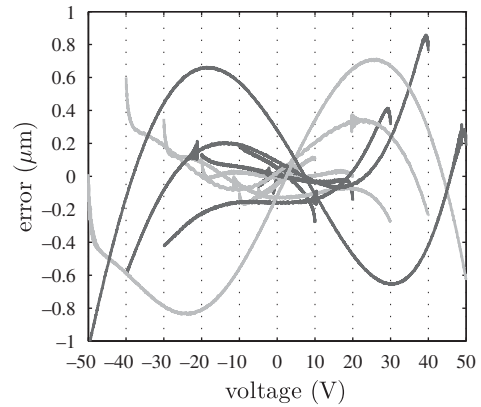


Fig. 7. Errors between the modeled and measured hysteresis of the trace (light grey) and retrace (dark grey) directions for various voltage ranges. Comparing the errors to the hysteresis curves of Fig. 3, it can be concluded that the model accurately describes the hysteresis of all voltage ranges.

retrace x_r ($\dot{V} < 0$) directions, different models are identified of which the parameters are given in Table II.

In Fig. 7 the errors between measured and modeled hysteresis are shown for various voltage ranges V_R . By comparing the hysteresis curves of Fig. 3 to the errors of Fig. 7, it can be seen that the model accurately describes the asymmetric hysteresis of the system. The model described by (4) with the trace/retrace parameters of Table II describes the hysteresis in the metrological AFM of all voltage ranges with an accuracy of 97%. This model will be used for the feedforward compensation, discussed in the next section.

IV. CONTROLLER DESIGN

Based on the RGA of Fig. 5, for controller design purposes the axes of the metrological AFM are assumed decoupled for frequencies $f < 100$ Hz. Using the measured FRFs of Fig. 4, three SISO controllers are designed using loopshaping techniques, all resulting in

Table III. The controller parameters and the resulting bandwidth, the phase margin and the amplitude margin for the different axes.

Axis	k	f_{LP} (Hz)	f_{BW} (Hz)	$\ S\ _{\infty}$ (dB)
x	0.07790	50	7.87	3.635
y	0.07790	50	8.03	4.052
z	0.1198	100	45.6	4.939

bandwidth frequencies $f_{BW} < 100$ Hz, *i.e.* where no coupling is present. Here, we use the definition bandwidth f_{BW} as the cross-over frequency of each diagonal loop gain $L_{ji}(f) = P_{ji}(f)C_{ji}(f)$, $i = j$, $i, j \in \{x, y, z\}$.

Moreover, for the x and y axes, position and hysteresis feedforward controllers are designed and applied separately. The performance of the hysteresis feedforward will be compared to the position feedforward in Section 5.2.

4.1 Feedback

Using the FRFs of the diagonal elements of (1), stabilizing feedback controllers C_{ji} , $i = j$, $i, j \in \{x, y, z\}$ are designed such that the modulus margin $\|S_{ji}(f)\|_{\infty} = \max_f |S_{ji}(f)| < 6$ dB, or

$$|S_{ji}(f)| = \left| \frac{1}{1 + P_{ji}(f)C_{ji}(f)} \right| \leq 6 \text{ dB}, \quad \forall f.$$

This corresponds to a phase margin $\phi \geq 30$ deg and an amplitude margin $A \geq 6$ dB. The controllers consist of an integrating action and a low-pass filter as

$$C_{ji}(s) = k \underbrace{\frac{1}{s}}_I \underbrace{\frac{2\pi f_{LP}}{s + 2\pi f_{LP}}}_{\text{low-pass}}, \quad (5)$$

where k denotes the controller gain and f_{LP} the cut-off frequency of the low-pass filter. In Table III, the controller parameters, the resulting bandwidths f_{BW} and the modulus margin $\|S\|_{\infty}$ for the different axes are shown. The margins are chosen somewhat higher to be robust against shifts in the resonance frequencies due to the nonlinearities in the piezo-stack actuators [4].

The characteristic loci $\lambda(PC)$ [24] of the SISO controlled MIMO system are shown in the right part of Fig. 8. The characteristic loci show that the controlled MIMO system has a good MIMO phase margin. The Nyquist plots of the separate diagonal loop gains, depicted in the right part of Fig. 8, almost coincide with the characteristic loci, *i.e.* $\lambda(PC) \approx \lambda(\text{diag}(PC))$. This again indicates that the different axes are almost decoupled. Furthermore, Fig. 8 shows that the diagonal loop gains are stable and do not enter the circle with

radius 0.5 centered at $(\text{Re}, \text{Im}) = (-1, 0)$, indicating that $\|S(f)\|_{\infty} < 6$ dB.

4.2 Hysteresis feedforward

The extended Coleman-Hodgdon model of (4) describes the position x as function of the applied voltage V . In order to use the model for a feedforward hysteresis compensation, expressions of the voltage as function of the position are required. These expressions equal

$$V(x) = \begin{cases} \frac{x - p_{4,t}}{p_{1,t}} - \frac{1}{p_{3,t}} \text{LW} \left(\frac{p_{2,t} p_{3,t}}{p_{1,t}} e^{\frac{p_{3,t}(x - p_{4,t})}{p_{1,t}}} \right), & \text{if } \dot{x} \geq 0 \\ \frac{x - p_{4,r}}{p_{1,r}} - \frac{1}{p_{3,r}} \text{LW} \left(\frac{p_{2,r} p_{3,r}}{p_{1,r}} e^{\frac{p_{3,r}(x - p_{4,r})}{p_{1,r}}} \right), & \text{if } \dot{x} < 0, \end{cases} \quad (6)$$

where LW denotes the LambertW function, which is the inverse of the function of $z(W) = We^W$, and

$$p_{1,t} = b_t - a_t e^{-c_t V_R},$$

$$p_{1,r} = b_r - a_r e^{-c_r V_R},$$

$$p_{2,t} = \frac{2(b_t - u_t)}{\alpha_t (e^{-\alpha_t V_m} + e^{-\alpha_t V_M})},$$

$$p_{2,r} = \frac{2(b_r - u_r)}{\alpha_r (e^{\alpha_r V_m} + e^{\alpha_r V_M})},$$

$$p_{3,t} = -\alpha_t, \quad p_{3,r} = \alpha_r,$$

$$p_{4,t} = -\frac{b_t - u_t}{\alpha_t} + d_t V_R^2 + e_t V_R + f_t,$$

$$p_{4,r} = \frac{b_r - u_r}{\alpha_r} + d_r V_R^2 + e_r V_R + f_r.$$

Equation (6) describes the required voltage as a function of the position x . If the input of (6) is chosen to be the reference position of the control loop r_x , the model can be used for feedforward control purposes. The model parameters of Table II are identified for the x direction of the metrological AFM. For the other axes, model parameters can be obtained in an analogous manner.

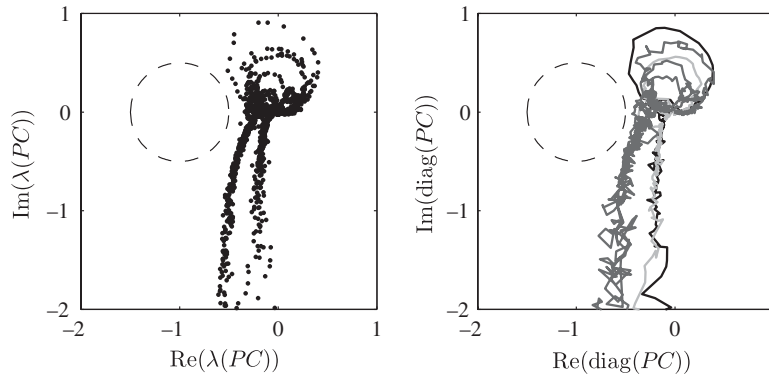


Fig. 8. Characteristic loci $\lambda(P(f)C(f))$ (left part) and Nyquist plots of the separate diagonal loop gains (right part) in x direction (black), y direction (dark grey) and z direction (light grey). The characteristic loci show that the SISO controlled MIMO system has a good phase margin and is stable. The resemblance between the two figures indicates that the axes are almost decoupled.

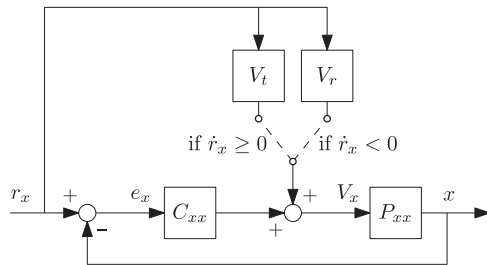


Fig. 9. Schematic representation of the hysteresis feedforward implementation. At the turnaround points where $\dot{r}_x = 0$, the hysteresis feedforward switches between the trace (V_t) and retrace (V_r) hysteresis feedforward or vice versa.

Since the hysteresis is asymmetric with respect to the trace and retrace direction, the hysteresis feedforward consists of two parts, one for each direction. The switch between the two parts $V_t(r_x)$ and $V_r(r_x)$ depends on the direction of the reference position, *i.e.* on the sign of the reference velocity. For increasing reference position r_x ($\dot{r}_x \geq 0$) the feedforward of the trace part $V_t(r_x)$ is used and for decreasing reference position r_x ($\dot{r}_x < 0$) the retrace hysteresis feedforward part $V_r(r_x)$ is used. The switch between the two hysteresis feedforward models is performed at standstill of the stage, *i.e.* outside the imaging region. A schematic overview of the implementation of the hysteresis feedforward for the x axis is shown in Fig. 9.

V. RESULTS

In this section, the results of the experiments on the metrological AFM are discussed. Scanning experiments are performed in x direction. The y direction is controlled to a constant position.

5.1 Hysteresis

The hysteresis feedforward of Section 4.2 is first tested in an open loop experiment. The reference trajectory is a forward and backward scan in x direction over a range of $\pm 18 \mu\text{m}$. The resulting voltage of the hysteresis feedforward, described by (6), is applied to the piezo-stack actuator in x direction. The reference position r_x , the stage position in x direction and the input voltage V are shown in Fig. 10. The resulting voltage of the feedforward (6) also has an offset and asymmetry in order to obtain the desired symmetric stage movement. The discontinuity at the turnaround point in the reference also results in a discontinuity in the hysteresis compensation due to the switching between the two models. This results in ringing of the positioning error. However, the ringing is reduced quickly by the feedback controller. The stage position x closely matches the reference position r_x , with a maximum absolute error $\max(|e_x|) = \max(|r_x - x|) = 0.2941 \mu\text{m}$.

5.2 Scanning motion

In Fig. 11, the results of a closed-loop experiment for a scan over $\pm 18 \mu\text{m}$ with a speed of $7.2 \mu\text{m/s}$ are shown. The use of only feedback control results in a tracking error of $\max(|e_x|) = 160.9 \text{ nm}$, as can be seen by the light grey line in Fig. 11.

Since the piezo-stack actuators act as position actuators, a position feedforward can be used to improve the performance of the stage [28]. The control input of the position feedforward can be added to the output of the feedback controllers V_i , $i \in \{x, y\}$, resulting in a new input to the system V_i^* as

$$V_i^*(t) = V_i(t) + K_i r_i(T), \quad i \in \{x, y\}, \quad (7)$$

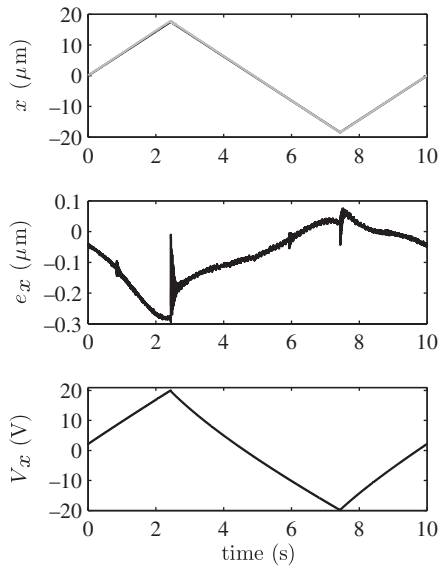


Fig. 10. Results of the open-loop hysteresis experiment, reference (black) and measured position (light grey), error and voltage resulting from the model. The stage position in x direction resembles the reference position r_x closely. The ringing of the error at the turnaround points is caused by the discontinuity of the hysteresis feedforward due to the switch between models.

where r is the reference signal and K the feedforward gain. The results for a closed-loop experiment with a position feedforward $K_x=K_y=11\text{ V}/\mu\text{m}$ are shown in Fig. 11 by the dark grey line. The position feedforward largely reduces the tracking error to $\max(|e_x|)=86.11\text{ nm}$.

The results of the experiment with feedback control and the hysteresis feedforward of Section 4.2 are shown in Fig. 11 by the black line. Compared to the position feedforward the hysteresis feedforward reduces the tracking error even further. The ringing of the input voltage due to the discontinuity by the switching of the hysteresis feedforward at the turnaround point results in a ringing of the tracking error. At these points, the feedback controller reduces the tracking error very quickly to the noise bound of $\pm 5\text{ nm}$.

The right part of Fig. 11 shows the square root of the cumulative power spectral densities (PSDs) of the tracking errors for the various experiments. For frequencies $f \rightarrow \infty$, the cumulative PSDs converge to the squared root-mean-square (rms) value of the respective errors. The rms values of the errors are for the experiment without feedforward $\text{rms}(e_{\text{no FF}}) = 99.57\text{ nm}$, with the position feedforward $\text{rms}(e_{\text{pos FF}}) = 19.34\text{ nm}$ and with the hysteresis feedforward $\text{rms}(e_{\text{hyst FF}}) = 11.08\text{ nm}$. The hysteresis feedforward added to the

feedback controller improves the tracking performance compared to using only the feedback control case with 89% and compared to the case with feedback control and position feedforward with 43%.

The sample topography, measured by the ZYGO interferometer in z direction, is shown as a function of the x position in Fig. 12. Since a triangular shaped reference in x direction is used, the topography of Fig. 12 contains the measured height of the sample for the scan in both positive and negative x direction. No large deviations in the measured height between the two directions can be seen. The measured topography shows a decaying height in x direction, indicating that the sample is tilted under the AFM. Since the output of the ZYGO interferometer is used instead of the control effort in z direction as is done in most literature, the height of the sample is directly measurable and traceable to the standard of length.

The reconstructed topography using the control effort in z direction is shown in Fig. 12 by the light grey line. The reconstructed topography clearly shows a global slope difference between the measured height by the ZYGO laser and the constructed height. This difference is likely to be caused by misalignments between the piezo-stack actuator and the ZYGO interferometer in z direction and by the fact that the piezo-stack actuator is not calibrated. Furthermore, a clear distinction can be made between the reconstructed height in positive and negative x direction as two lines are visible. The control effort in z direction also contains influences of the hysteresis and creep of the piezo-stack actuators and the small amount of coupling between the different DOFs. This causes the errors in the constructed topography image. Further postprocessing of the data in combination with an accurate system model is required to better reconstruct the sample topography from the control effort in z direction.

During the experiment, the y axis is controlled to a fixed position. The tracking error in y direction is shown in Fig. 13 together with the control effort. The shape of the control effort of Fig. 13 clearly shows a correlation with the sample topography of Fig. 12. Based on the FRF of the system (see Fig. 4) a coupling of 1% between the axes was expected for frequencies $f < 100\text{ Hz}$. The cumulative PSD of e_y , shown in the right of Fig. 13, converges for $f \rightarrow \infty$ to 4.83 nm , so $\text{rms}(e_y) = 2.20\text{ nm}$.

5.3 Scanning speed

The tracking errors are dependent on the scanning speed. Real-time imaging of the sample is only

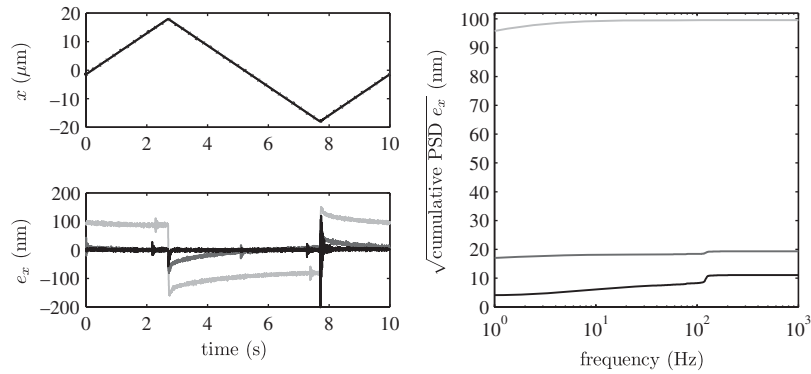


Fig. 11. Measured positions, tracking errors and square root of the cumulative PSDs of the tracking errors in x direction for the closed loop experiments, reference (dotted), without feedforward (light-grey), with position feedforward (dark-grey) and with the hysteresis feedforward (black). The hysteresis feedforward improves the tracking performance with 89% compared to the feedback only case and with 43% compared to the feedback with position feedforward case.

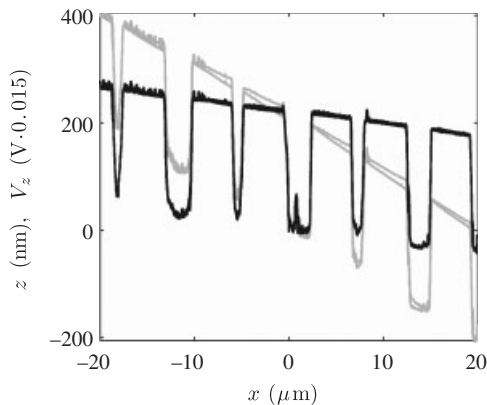


Fig. 12. Measured topography of the sample with the ZYGO interferometer (black) and constructed topography using the control effort in z direction (grey). Misalignment and calibration issues cause the reconstructed topography to show an additional global slope. Also, the reconstructed topography shows a difference between the trace and retrace direction, which is not present in the direct topography measurement.

possible if the scanning movement is controlled within the sensor noise bound during the imaging periods, except for the turning points where no image is made. The rms values of the tracking errors for experiments with feedback and hysteresis feedforward control are shown in Table IV for various scans speeds. The error increases with increasing scanning speed. In order to increase the scanning speed, the tracking errors have to be reduced. One possible solution is the increase of the bandwidth of the system. However, this would require MIMO control since decoupling of the axes is no longer guaranteed when increasing the bandwidth f_{BW} much further (Fig. 5).

VI. CONCLUSIONS

Using a full non-parametric MIMO model of the system, the coupling between the different axes has been investigated using the frequency dependent relative gain array (RGA). The RGA shows that for feedback controller design the axes can be considered to be decoupled up to a frequency of 100 Hz.

For all DOFs separately, feedback controllers are designed using loopshaping techniques and resulting in bandwidth frequencies below which the coupling effects may be disregarded for the feedback control design. The characteristic loci show that the SISO controlled MIMO system has a good MIMO phase margin.

An extended Coleman-Hodgdon model containing a scan range dependent offset has been identified in x direction for the trace and retrace directions separately to account for the asymmetry in the hysteresis. The generic extended model describes the hysteresis with an accuracy of 97%. Similar models can be identified for the other axes.

A hysteresis feedforward has been made using two different extended Coleman-Hodgdon models, one for the trace and one for the retrace direction. The switch between the models is done at standstill of the stage. The application of the hysteresis feedforward improves the tracking performance by 89% compared to using only feedback control and by 43% compared to using feedback control and a position feedforward.

With the presented control method, the AFM can perform scanning movements with a velocity up to $3.6 \mu\text{m/s}$ and a tracking error within the sensor bound of $\pm 5 \text{ nm}$. A separate laser is used to measure the sample topography directly through the stage movement in

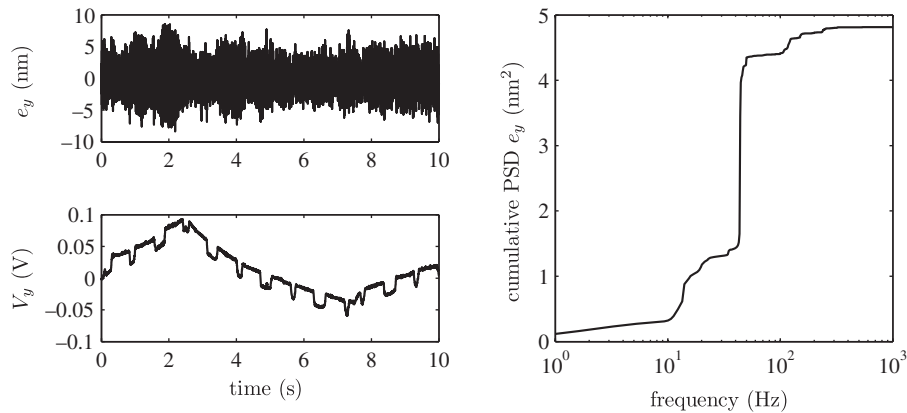


Fig. 13. Tracking error (left top), control effort (left bottom) and cumulative PSD (right) in y direction. A clear correlation between the control effort in y direction and the sample topography of Fig. 12 can be seen, indicating a coupling between the axes.

Table IV. Root-mean-square (rms) values of the tracking errors for varying reference speeds.

Speed ($\mu\text{m/s}$)	3.6	7.2	14.4	28.8
$\text{rms}(e_x(t))$ (nm)	7.317	11.08	14.38	23.28

vertical direction. Sample images are obtained with a sensor bound of 2 nm.

Although for controller design purposes the system is assumed decoupled for frequencies $f < 100$ Hz, still 1% coupling is present in the performance. Furthermore, the position measurements of the stage in all DOFs suffer from disturbances, which deteriorate the achievable performance of the AFM. In future research, MIMO control methods will be employed to further increase the bandwidth and with this the achievable scanning speed and to account for the disturbances acting on the MIMO system.

Reduction of the discontinuity of the hysteresis feedforward at the switching instances is also subject of further research. Reduction of the discontinuity is expected to result in a reduction of the ringing in the input voltage and an improved positioning accuracy.

REFERENCES

1. Binning, G., C. F. Quate, and C. Gerber, "Atomic force microscope," *Phys. Rev. Lett.*, Vol. 56, No. 9, pp. 930–933 (1986).
2. Schitter, G., "Advanced mechanical design and control methods for atomic force microscopy in real-time," *Am. Control Conf.*, New York, pp. 3503–3508 (2007).
3. Pao, L. Y., A. Butterworth, and D. Y. Abramovich, "Combined feedforward/feedback control of atomic force microscopes," *Am. Control Conf.*, New York, pp. 3509–3515 (2007).
4. Sebastian, A. and S. M. Salapaka, "Design methodologies for robust nano-positioning," *IEEE Trans. Control Syst. Technol.*, Vol. 13, No. 6, pp. 868–876 (2005).
5. Stemmer, A., G. Schitter, J. M. Rieber, and F. Allgöwer, "Control strategies towards faster quantitative imaging in atomic force microscopy," *Eur. J. Control*, Vol. 11, No. 4–5, pp. 384–395 (2005).
6. Salapaka, S., A. Sebastian, J. P. Cleveland, and M. V. Salapaka, "Design, identification and control of a fast nanopositioning device," *Am. Control Conf.*, Alaska, Vol. 3, pp. 1966–1971 (2002).
7. Zou, Q. and S. Devasia, "Preview-based optimal inversion for output tracking: application to scanning tunneling microscopy," *IEEE Trans. Control Sys. Technol.*, Vol. 12, No. 3, pp. 375–386 (2004).
8. Daniele, A., S. Salapaka, M. V. Salapaka, and M. Dahleh, "Piezoelectric scanners for atomic force microscopes: design of lateral sensors, identification and control," *Am. Control Conf.*, San Diego, Vol. 1, pp. 253–257 (1999).
9. Humphris, A., M. Miles, and J. Hobbs, "A mechanical microscope: High-speed atomic force microscopy," *Appl. Phys. Lett.*, Vol. 86, No. 3, pp. 034106 (2005).

10. Ando, T., N. Kodera, E. Takai, *et al.*, “A high-speed atomic force microscope for studying biological macromolecules,” *Proc. Nat. Acad. Sci.*, Vol. 98, No. 22, pp. 12 468–12 472 (2001).
11. Kindt, J. H., G. E. Fantner, J. A. Cutroni, and P. K. Hansma, “Rigid design of fast scanning probe microscopes using finite element analysis,” *Ultramicroscopy*, Vol. 100, No. 3–4, pp. 259–265 (2004).
12. Schitter, G., G. E. Fanter, P. J. Thurner, J. Adams *et al.*, “Design and characterization of a novel scanner for high-speed atomic force microscopy,” *IFAC Mechatron. Conf.*, pp. 819–824 (2006).
13. *P-517, P-527 Multi-Axis, Piezo Nanopositioning/ Scanning Stages with Parallel Metrology*, Physik Instrumente, www.physikinstrumente.com.
14. Schitter, G., P. Menold, H. F. Knapp, F. Allgöwer *et al.*, “High performance feedback for fast scanning atomic force microscopes,” *Rev. Sci. Instrum.*, Vol. 72, No. 8, pp. 3320–3327 (2001).
15. Song, J. and A. d. Kiureghian, “Generalized Bouc–Wen model for highly asymmetric hysteresis,” *J. Eng. Mech.*, Vol. 132, No. 6, pp. 610–618 (2006).
16. Smith, R., M. Salapaka, and L. Cherveny, “A Preisach model for quantifying hysteresis in an atomic force microscope,” *SPIE Smart Structures and Materials*, pp. 7 (2002).
17. Jang, M., C. Chen, and J. Lee, “Modeling and control of a piezoelectric actuator driven system with asymmetric hysteresis,” *IEEE Int. Conf. Syst. Signals*, Kaoshiung, Taiwan, pp. 676–681 (2005).
18. Kwok, N. M., Q. P. Ha, M. T. Nguyen, J. Li *et al.*, “Bouc-Wen model parameter identification for a MR fluid damper using computationally efficient GA,” *ISA Trans.*, Vol. 46, No. 2, pp. 167–179 (2007).
19. Lin, C. and S. Yang, “Precise positioning of piezo-actuated stages using hysteresis-observer based control,” *Mechatronics*, Vol. 16, No. 7, pp. 417–426 (2006).
20. Dirscherl, K., J. Garnæs, L. Nielsen, J. Jørgensen *et al.*, “Modeling the hysteresis of a scanning probe microscope,” *J. Vac. Sci. Technol. B*, Vol. 18, No. 2, pp. 621–625 (2000).
21. Yang, Q. C. Ftaclas, M. Chun, and D. Toomey, “Hysteresis correction in the curvature adaptive optics system,” *J. Opt. Soc. Am. A*, Vol. 22, No. 1, pp. 142–147 (2005).
22. Moheimani, S. O. R. and A. J. Fleming, *Piezoelectric Transducers for Vibration Control and Damping*, ser. Advances in Industrial Control, Grimble, M. J. and M. A. Johnson, Eds. Springer, London (2006).
23. Ljung, L., *System Identification: Theory for the User*, 2nd ed., Prentice-Hall, Upper Saddle River, New Jersey, (1999).
24. Skogestad, S. and I. Postlethwaite, *Multivariable Feedback Control, Analysis and Design*, 2nd ed., John Wiley & Sons, West Sussex, England, (2005).
25. Bristol, E., “On a new measure of interaction for multivariable process control,” *IEEE Trans. Autom. Control*, Vol. 11, No. 1, pp. 133–134 (1966).
26. Coleman, B. D. and M. L. Hodgdon, “A constitutive relation for rate-independent hysteresis in ferromagnetically soft materials,” *Int. J. Eng. Sci.*, Vol. 24, No. 6, pp. 897–919 (1986).
27. Dirscherl, K., “Online correction of scanning probe microscopes with pixel accuracy,” *PhD Thesis*, Technical University of Denmark (August 2000).
28. Merry, R., M. Uyanik, K. Koops, M. v. d. Molengraft *et al.*, “Modeling, identification and control of a metrological atomic force microscope with a 3d of stage,” *Am. Control Conf.*, Seattle, Washington, pp. 2716–2721 (2008).



Roel J. E. Merry received the M.Sc. degree (cum laude) in mechanical engineering from the Eindhoven University of Technology (TU/e) in 2005. Currently he is a PhD student in the Control Systems Technology group of the Department of Mechanical Engineering at the TU/e. His research focusses on the identification and control of nano-motion systems driven by piezoelectric actuators and on the extraction of accurate signal estimations from optical incremental encoders.



Mustafa Uyanik received the Bachelor degree in Mechanical Engineering from the Hogeschool Brabant in 2002 and is currently a Master student in the Control Systems Technology group of the Department of Mechanical Engineering at the Eindhoven University of Technology. His research interests are the identification and

control of motion systems, with a special focus on atomic force microscopes.



Marinus (René) J. G. van de Molengraft received the M.Sc. degree (cum laude) in mechanical engineering from TU/e in 1986, and the Ph.D. in 1990 on identification of mechanical systems for control. Since 1992, he has been an assistant professor in the Control Systems Technology group of the Department of Mechanical Engineering at TU/e. His current research interests are real-time control of embedded motion systems and the integrated design of mechatronic systems.

His current research interests are real-time control of embedded motion systems and the integrated design of mechatronic systems.



Richard Koops is a scientist working in the field of nanometrology. He received his Ph.D. degree at the University of Groningen, The Netherlands, in 1992 for work on a scanning tunneling microscope for surface physics research. After several postdoc positions at Delft University of Technology he joined NMI Van Swinden Laboratory in Delft in 1999. Since then he is working at NMI in the field of length metrology as a specialist in scanning probe metrology.

Since then he is working at NMI in the field of length metrology as a specialist in scanning probe metrology.



Marijn G. A. van Veghel received the M.Sc. degree (cum laude) in experimental physics from Utrecht University, The Netherlands, in 1999, and a Ph.D. in surface physics in 2004, also from Utrecht University. Since 2005, he is employed as a scientist in the length section of NMI Van Swinden Laboratory in Delft, which is the

Dutch national metrology institute. His current research topics are scanning probe microscopy and co-ordinate metrology at micro- and nanometer levels.



Maarten Steinbuch received the M.Sc. degree (cum laude) and the Ph.D. degree from the Delft University of Technology, in 1984 and 1989, respectively. From 1987 to 1999 he was with Philips Labs., Eindhoven. Since 1999 he is full professor and head of the Control Systems Technology group of the Mechanical Engineering Department of Eindhoven University of Technology. His research interests are the modeling, design and control of motion systems and automotive powertrains. Since July 2006 he is also Scientific Director of the 3TU Centre of Competence High Tech Systems of the Federation of Dutch Technical Universities. He is Editor-in-Chief of IFAC Mechatronics.

His research interests are the modeling, design and control of motion systems and automotive powertrains. Since July 2006 he is also Scientific Director of the 3TU Centre of Competence High Tech Systems of the Federation of Dutch Technical Universities. He is Editor-in-Chief of IFAC Mechatronics.